Additive Manufacturing 89 (2024) 104294

Contents lists available at ScienceDirect

Additive Manufacturing

journal homepage: www.elsevier.com/locate/addma

Research Paper

Deformation constrained support-structure optimization for laser powder bed fusion

Subodh C. Subedi [a], Dan J. Thoma [b,a], Krishnan Suresh [a,*]

[a] Mechanical Engineering Department, University of Wisconsin-Madison, USA
[b] Material Science & Engineering Department, University of Wisconsin-Madison, USA

ARTICLE INFO

Keywords:
Laser powder bed fusion
Truss supports
Frame support structures
Design optimization
Part deformation
Inherent strain
Multi-load
Coupled Analysis

ABSTRACT

Support structures act as primary conduits for heat flow in laser powder bed fusion (LPBF). Frame supports, as opposed to block-type supports, have proven to be a good choice for LPBF, with no metal powder entrapment and ease of removal. In this paper, we use a multi-load formulation, where different loads at different instances of time are used for frame support optimization, to constrain the structural deformation of the part during printing. Parts and supports are analyzed in tandem at the end of each layer build, to account for the role of support stiffness in the overall part deformation. The proposed framework prevents recoater collision, and controls the geometric accuracy of the part, by optimizing the size of frame supports. Numerical results for the optimal volume of manufacturable frame support are reported for geometries with varying overhang characteristics.

1. Introduction

Support structures are essential to several additive manufacturing processes such as Laser Powder Bed Fusion (LPBF), Fused Deposition Modeling (FDM), and Stereolithography (SLA), where the feed-stock material does not provide sufficient structural support and/or thermal conduit. In FDM, overhang surfaces, at or over a predefined threshold inclination angle (usually 45°) with the build direction, require support to prevent collapse under gravity. However, in LPBF, the major role of supports is thermal management. Fig. 1 illustrates both external and internal overhang surfaces that require supports. In LPBF, large thermal gradients from rapid heating and cooling induce residual stresses. This, in turn, leads to part defects [1,2] such as plastic distortions, warping, delamination, cracks, and part-deformation-induced recoater collision. The supports provide thermal pathways for transferring the heat from melt-pool to the build plate since the powder has less than 10% lesser thermal conductivity compared to the solid [3]. These thermal pathways reduce heat accumulation by swiftly transferring the heat to the build plate (sink) while providing mechanical resistance to thermal deformations [4]. In addition, supports also enhance the surface finish [5]. The focus of this paper is the optimal design of support structures to prevent such failures [6–8]. Alternate methods to minimize residual stresses and part distortion involve the use of optimal scan strategies [9–11], build direction [12,13], optimal process parameters [14,15], and support-less manufacturing [16,17].

1.1. Support optimization

Supports are usually built with lesser energy (<40%), larger layer thickness ($2X$), and faster print speed compared to the part being built. This reduces time, material, and post-processing costs. Yet, a significant amount of cost is associated with support structures today, accounting for upwards of 40%, depending on the part geometry and build configuration [18]. This strongly motivates the need to minimize the amount of support used and to minimize the powder entrapped within these supports. Support minimization can be carried out, for example, by build direction optimization [19], geometry compensation [19,20], continuous feedback control [16,21,22], design for additive manufacturing (DfAM) rules [23], and/or using open structured support design [7]. In this paper, we will assume that these have been implemented, but a further reduction in support and entrapped powder is desired while ensuring part printability.

Towards this end, we list the main challenges underlying physics-based LPBF support optimization.

- **Simplified Analysis**: LPBF is an extremely complex process involving multiple physics, multiple length scales, and multiple time scales. It is virtually impossible to consider every aspect of the LPBF process during support structure optimization. Instead, a thermal or structural analysis, with some level of simplification, is carried out to reduce the computational cost. Simplified analysis involves the use of representative volume element

* Corresponding author.
E-mail address: ksuresh@wisc.edu (K. Suresh).

https://doi.org/10.1016/j.addma.2024.104294
Received 22 November 2023; Received in revised form 17 May 2024; Accepted 2 July 2024
Available online 5 July 2024

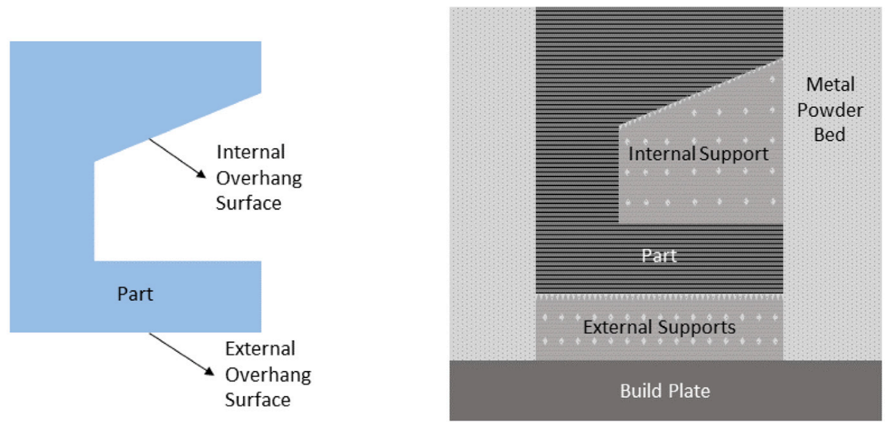

(a) *Part with overhang surfaces* (b) *Part build with supports*

Fig. 1. Support structures in LPBF-based metal additive manufacturing.

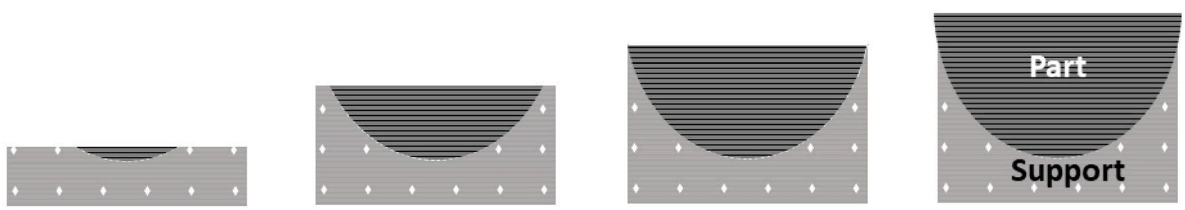

Fig. 2. Support evolution in LPBF.

(RVE) [24], linear-elastic material assumptions [25], layer lumping [26], and many more. In this regard, we discuss below various simplifications that have been proposed for efficient support optimization.

- **Design Variables**: The primary support optimization strategies are either topology optimization, where pseudo-density variables serve as the design variables [27], or size optimization, where the thickness of the support members serves as the design variables [7]. In either case, one must observe that the supports are evolving during the LPBF process (see Fig. 2), making support structure optimization unique and challenging. The design domain and the heat input changes, at each layer, as parts and supports evolve. This contrasts with classic structural optimization [28,29], where the underlying structure does not evolve with time. Researchers often chose to disregard the evolving aspects of support geometry, and instead, consider only the final support geometry.
- **Objective**: One of the primary goals of support optimization is to minimize part failures. Authors typically focus on either a thermal objective (for example, minimizing the temperature or thermal compliance) or a structural objective (for example, minimizing part deformation or structural compliance).
- **Constraints**: LPBF has several inherent constraints; these include material usage, printing time, powder entrapment, and post-processing (i.e., support removal).
- **Validation**: Since several assumptions are typically involved in support structure optimization, the numerical results should, if possible, be supported through experiments.

An overview of the existing approaches towards support optimization is provided next, based on the characteristics discussed above.

1.2. Literature review

Most of the prior work [27,30–34] on support structure optimization are targeted towards FDM, where supports prevent the collapse of overhang surfaces and have no functional role in thermal management. For LPBF, Javidrad and Javidrad [35] review various topology optimization (TO) methods for their merits and shortcomings. As summarized in the review, existing methods do not guarantee optimal support. For an additional review of LPBF support optimization based on physical experiments and geometric rules, please see [7]. Zhou et al. [36] designed self-supporting and easy-to-remove supports by integrating additive manufacturing constraints in topology optimization (TO). A transient thermal analysis was carried out and a finite number of points were selected for monitoring the temperature. TO of the overhang support volume was carried out to minimize these temperature values. However, only 2D results were presented, and the points were arbitrarily chosen. Weber et al. [37] optimized geometric parameters of tree-like supports to minimize part deformation in LPBF. The simulations produced a Pareto frontier for support volume against the part's maximum displacement. Physical experiments exhibited a reduction in part deformation; the supports were generated manually, specifically for a rectangular overhang surface. Allaire and Bogosel [38] proposed a framework for multi-phase optimization of part orientation, shape, and topology of supports to minimize average thermal and structural compliances, subjected to overhang constraints and constant heat flux loads; only numerical results were presented. Wang and Qian [39] used a constant heat flux-based loading on the boundary of overhang surfaces to optimize the topology of supports for maximizing heat dissipation. The effect of the layer-wise build as well as the thermal resistance of the supports was not included. Malekipour et al. [40] also used uniform heat flux distribution over the overhang surfaces to generate optimal supports that maximize heat conduction. Multiple geometries were generated and the one with maximum heat conduction and least material was selected as the optimal design. Pellens et al. [41] used inherent strain-based loading on each part layer to limit the vertical displacement of the overhang surface. Topology optimization was carried out to generate optimized lattice supports. However, the effect of the layer-wise build was not accounted for during the analysis and optimization process.

Huang et al. [42] used a simplified heat transfer model to optimize the topology of lattice supports for minimizing thermal compliance. The assumption of constant heat distribution over the overhang surfaces is inconsistent with the transient nature of the LPBF process. Cheng et al. [43] used inherent strain-based loading to generate graded periodic lattice supports using topology optimization. However, these methodologies fail to incorporate the effect of the layer-wise build process. Amir and Amir [44] minimized weighted compliance due to body forces obtained from intermediate stages of layer-wise build simulation to generate parts and supports with solid-void and void-lattice-solid parametrization. However, supports were not accounted for during the process simulation. Bartsch et al. [45] optimized supports for heat dissipation using maximum temperature distribution obtained from layer-wise thermal simulation of a part until the first overhang layer. TO of the design domain constructed using an overhang surface was carried out to generate supports. This method does not incorporate the entire build history of the part. Miki and Nishiwaki [46] used layer-wise build simulation to obtain aggregate thermal loads to optimize support; however, the work did not account for thermal resistance of supports. Topology optimization of supports was carried out by Zhang et al. [47], to minimize the structural compliance for given support volume fraction constraints. Parallel computing was employed to speed up topology optimization of supports, subjected to a weighted sum of structural compliances due to gravity load and inherent strain-based loads. Experimental results showed a significant reduction in part deflections and a reduction in material usage. However, the results were presented for a simple cantilever beam, i.e., support evolution was not considered. Equivalent static load-based optimization of lattice supports was carried out by Lee and Yun [48], which incorporates the effect of layer-wise part-built thermal history into the optimization framework. The effective part-scale thermal load, obtained using a liquid lifetime of a melt pool was used to compute thermal energy distribution. Results for a twin cantilever beam with graded lattice support were presented. The authors of this paper used aggregate equivalent static loads computed from layer-wise build simulation to generate frame supports [7], which were optimized for minimal thermal compliances. The supports were optimized for a single load that exhibited the worst loading case.

In all of the above, the contribution of structural and thermal stiffness of supports during the part-build process is neglected. More recently, Dugast and To [49] used layer-wise inherent-strain based elasto-plastic finite element simulation to optimize support topology. However, the optimized support topologies have numerous model reconstruction and manufacturing challenges [50].

In summary:

1. Most prior works consider a constant structural/thermal load at the overhang surface to generate supports.
2. Supports are generated after the part-build simulation, where the thermal resistance and structural stiffness of supports are excluded from the analysis.
3. The results for support analysis and optimization are presented for a fixed support geometry (for example, a cantilever beam). Supports for a generic part where supports evolve with the geometry are typically not considered.
4. Amount of support material required for part printing is often identified using a simple projection, which does not necessarily provide the optimal distribution of material within the support volume.

1.3. Paper contributions

With these research gaps in mind, we propose to optimize the evolving supports using a multi-load strategy that accounts for varying support loads during the build process. The load at each layer is determined using inherent-strains. As each layer is built, only the active supports are analyzed. In particular, frame supports are used here since (1) they do not entrap powder, (2) they can be easily optimized, and (3) they are easy to remove. The support volume is minimized subject to two sets of nodal deformation constraints: (1) the vertical deformation is constrained to avoid recoater collisions, and (2) the total deformation is constrained to minimize part deformation (i.e., improve part accuracy). The design variables are the cross-sectional areas of the frame supports.

2. Proposed strategy

The proposed strategy is presented in Fig. 3, and is described in the remainder of this section.

2.1. Frame support generation

The first step in the proposed strategy is to generate frame support structures. This is purely based on the need for support at any point on the part surface. Parts used in this work are represented by tessellated surface triangles. For a given part build configuration (part placement, build direction, and part orientation), the overhang surface is identified based on the inclination of surface triangles with the build direction.

Using the vertices of these surface triangles, self-supporting frame supports are generated; see [7,8] for details. The support topology is defined by the inter-comb distance (D), the comb height (C_h), the part clearance height (H_{min}), the threshold support angle (θ_s), and the support angle for frame (θ_t), as shown in Fig. 4(a). Typical frame support for a hemisphere is shown in Fig. 4(c). The hexmeshed part and corresponding frame supports are coupled for analysis (discussed later), resulting in penetrating beam elements. The support generation relies on the resolution of geometry. However, the greedy algorithm ensures adequate self-support with the minimum number of members for part manufacturability.

Unlike other frame designs [51–53], these supports have proven to work for LPBF [7]. They do not entrap metal powder, and owing to their thin cross-section thickness, they can be easily removed during post-processing. Frame supports with optimized cross-section area are converted to triangles with implicitly defined thickness using the workflow shown in Fig. 5(a). Hemisphere with convex overhang surface manufactured with frame supports is shown in Fig. 5(b).

Observe that the support evolves along with the part during a part-print process, as illustrated in Fig. 6. At intermediate stages, some frame members are built but do not participate in the heat transfer since they are not connected to the overhang surface, as seen in Figs. 6(a) and 6(b). Once the overhang surface ends, the entire frame support remains active throughout the part build process, as seen in Figs. 6(c) and 6(d). This observation is critical for the simulation of part and support printing.

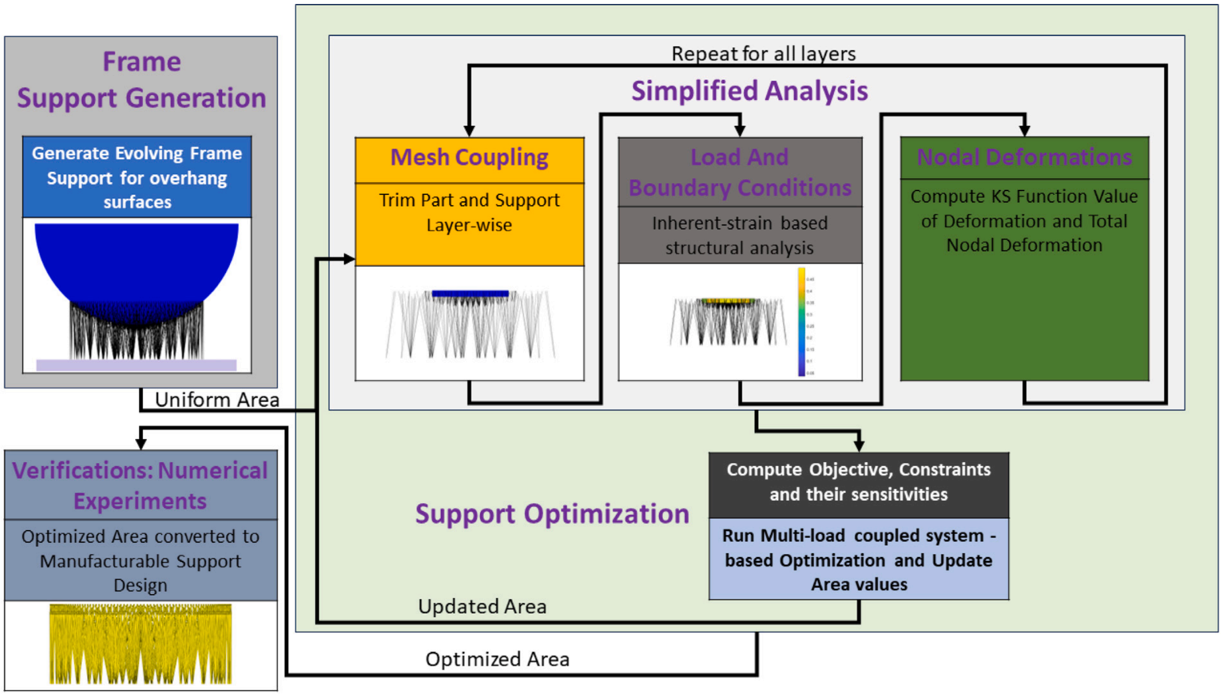

Fig. 3. Proposed strategy to optimize evolving supports with multi-loads.

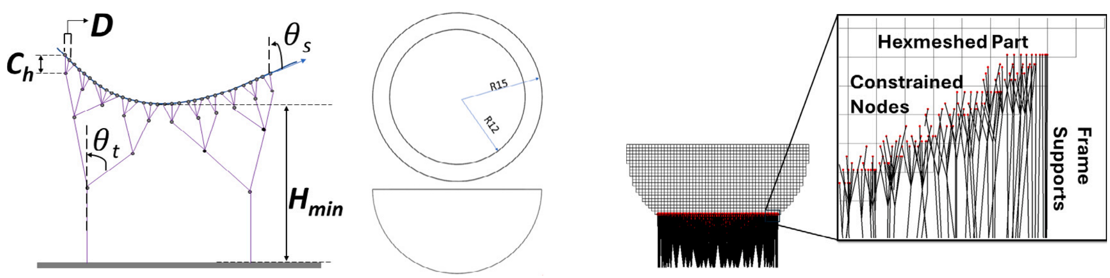

(a) *Support details.* (b) *Hemisphere details* (c) *Part with Frame supports.*

Fig. 4. Frame support details; hemisphere dimensions are in mm.

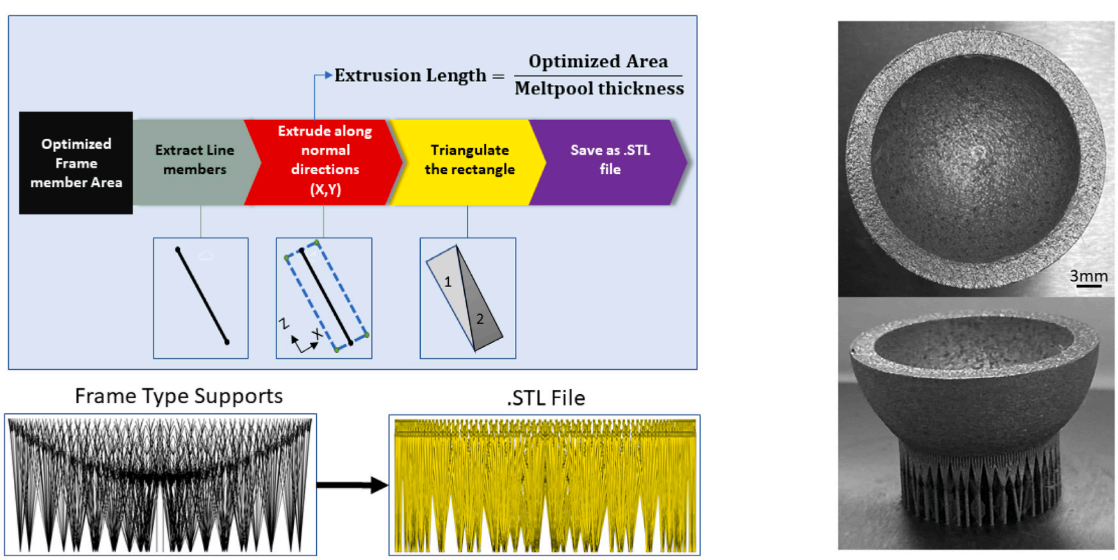

(a) *Conversion of Frame support to .STL file* (b) *Printed Part*

Fig. 5. Optimized frame support for a hemisphere.

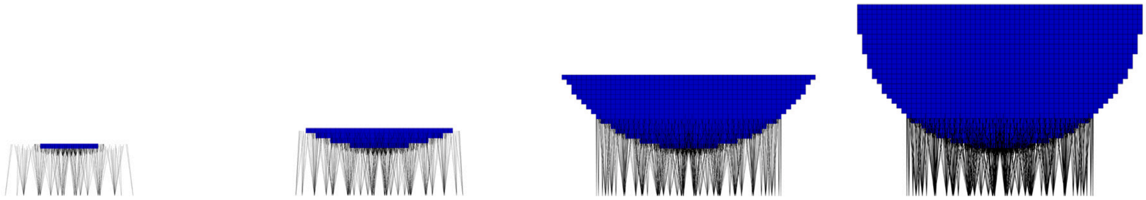

(a) (b) (c) (d)

Fig. 6. Support evolution for overhang surface.

2.2. Simplified analysis

As mentioned earlier, simplified analysis is essential for downstream optimization. Various steps of the proposed simplified analysis are discussed next.

2.2.1. Mesh-coupling

The part is meshed using uniform hexagonal elements, i.e., voxels. The size of each voxel is chosen to be around 10–20 times the powder layer thickness. The supports are 1D beam elements, with associated cross-sectional areas. The part and support are trimmed for each layer to simulate the layer-wise build process. The 3D voxel nodes and 1D support nodes are coupled based on their proximity; see [7] for details. Only translational degrees of freedom of the beam element nodes are coupled with the hexagonal elements based on their proximity. The rotational degrees of freedom of the beam elements at the interface are indirectly constrained by the penetrating nature of these elements. The elemental structural stiffness matrices of the trimmed part (k_{hex}) and trimmed frame (k_{frame}) are computed and assembled to form global stiffness matrices $\hat{K}_{hex}$ and $\hat{K}_{frame}$. The well-known analytical expression for k_{frame} is used [54], while k_{hex} is computed as follows:

$$\left[k_{hex}\right] = \int_{\Omega_e} [\nabla N_{hex}]^T [D_{hex}][\nabla N_{hex}]\, d\Omega_e \tag{1}$$

where N_{hex} are the finite element voxel shape functions, and D_{hex} are the voxel element constitutive matrices. For computational efficiency, material properties used in computing these matrices, are assumed to be independent of temperature. The global coupled stiffness matrix K, given by Eq. (2), is an assembly of $\hat{K}_{hex}$ and $\hat{K}_{frame}$, and involves the coupling matrix C:

$$K = \begin{bmatrix} \hat{K}_{hex} & 0 & \\ 0 & \hat{K}_{frame} & C^T \\ & C & 0 \end{bmatrix} \tag{2}$$

Note that computing $\hat{K}_{frame}$ requires the cross-section area and moment of inertia of the frame [54]. All frame members are initially assigned the same cross-sectional area that is calculated based on the initial support volume assigned. The cross-section is assumed to be four-finned to provide high buckling resistance, while the ends are assumed to be octagonal (see Fig. 7) since this enables good heat transfer, and easy removal [7]. The thickness of each frame member is designed to be the melt pool thickness t; therefore, the web length b_e is directly related to the cross-sectional area and t.

2.2.2. Load and boundary conditions

As discussed earlier, numerous simplified loading strategies have been explored. Some researchers have used resource-intensive models to simulate the heat transfer during laser-powder interactions at elemental scale [36,55], while others have used more efficient flash heating of each layer [7,56,57], or equivalent structural loading for purely mechanical analysis [58–60].

In this paper, we consider a layer-scale inherent-strain-based loading to compute part and support deformation. Inherent strains originating in welding [61,62] are now used in LPBF. A recent review by Mohammadtaheri et al. [63] provides an in-depth overview of the inherent strain approach in LPBF. The inherent strain in the heat affected zone (HAZ) is composed of plastic strain, thermal strain, strain due to phase change and creep [59,64,65]:

$$\begin{aligned} \varepsilon^{inh} &= \varepsilon^{total} - \varepsilon^{elastic} \\ \varepsilon^{inh} &= \varepsilon^{thermal} + \varepsilon^{plastic} + \varepsilon^{phaseChange} + \varepsilon^{creep} \end{aligned} \tag{3}$$

Inherent strains are computed through numerical simulations of a single laser track [66,67] or a small representative volume element (RVE) [24,60,65,68] for a given set of material and process parameters. Recent work by Park et al. [69] incorporates the effect of multiple layers in a part to compute inherent strain at each layer. Layerwise inherent strains (ε_l^{inh}) generated for a given layer (l), are functions of number of layers (l), the layer thickness (H), depth that affects the inherent strain (r), and the inherent strain for the first layer (ε^{inh}). Layerwise inherent strains are given by,

$$\varepsilon_l^{inh} = l\varepsilon^{inh} - \frac{(l-1)r}{H}\varepsilon^{inh} \tag{4}$$

Layerwise equivalent structural loads are computed using inherent strains from Eq. (4). These loads are uniformly applied to all elements of the topmost hex mesh layer of each active coupled system. The frame nodes in contact with the build plate are assigned a zero-Dirichlet boundary condition. The loads and boundary conditions are assembled as follows:

$$\begin{aligned} \{f_{hex}^l\} &= \int_{\Omega_e} [\nabla N_{hex}]^T [D_{hex}]\varepsilon_l^{inh}\, d\Omega_e \\ \{F^l\} &= \begin{Bmatrix} f_{hex}^l \\ f_{frame}^l \\ 0 \end{Bmatrix} \\ \{d^l\} &= \begin{Bmatrix} d_{hex} \\ d_{frame} \\ \lambda \end{Bmatrix} \end{aligned} \tag{5}$$

where f_{hex}^l captures the equivalent structural loads computed using layerwise inherent strains ε_l^{inh}, f_{frame}^l are the zero loads on the frame nodes, and λ's are the Lagrange multipliers. For every active coupled system simulating a new layer built, the following linear system is solved:

$$[K^l]\{d^l\} = \{F^l\} \tag{6}$$

The FEA engine uses a direct solver with linear elastic material and small strain assumption. The total nodal displacement and vertical displacements obtained from the finite element solutions are agglomerated to use them as constraints in optimization.

2.2.3. Nodal deformations

Part deformation in LPBF adversely affects geometric accuracy, as well as the build process. Specifically, if the vertical deformation exceeds the powder layer height, it might lead to recoater collision, disrupting powder deposition and potentially damaging the entire part, as illustrated in Fig. 8(a). Similarly, the total deformation adversely affects part deviation from the ideal geometry as shown in Fig. 8(b).

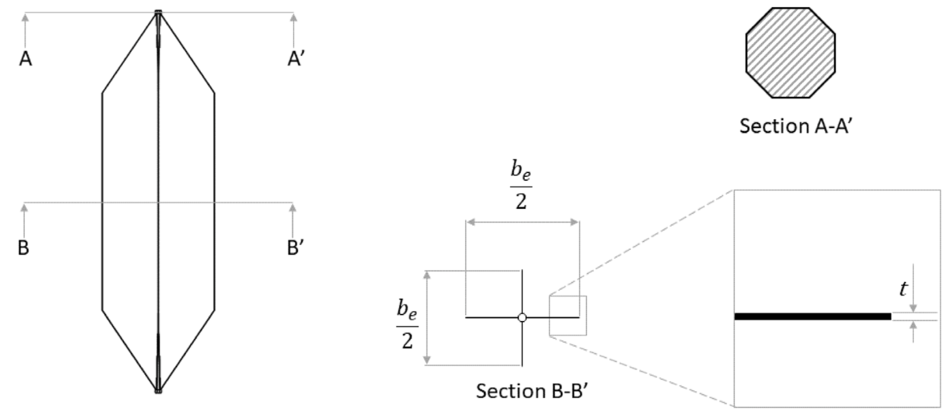

Fig. 7. Details of frame member cross-section [7].

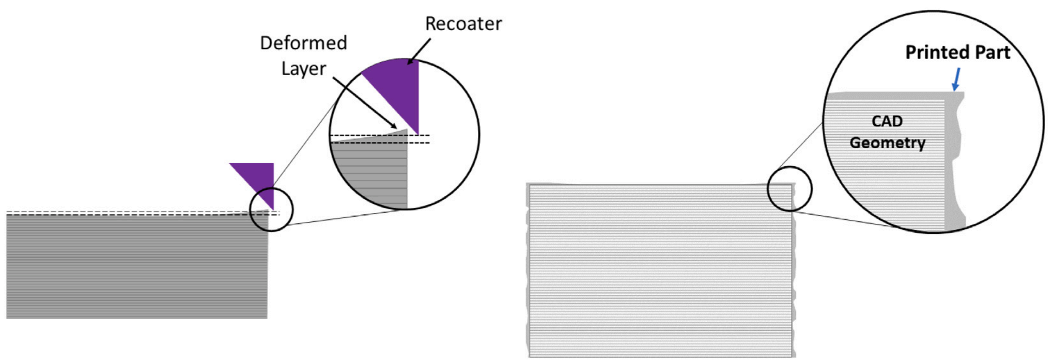

(a) *Vertical Deformation* (b) *Total Deformation*

Fig. 8. Deformation constraints.

Thus, we must consider two sets of constraints:

$$\begin{aligned} w_j &\leq \hat{w} \\ \delta_j &\leq \hat{\delta} \end{aligned} \tag{7}$$

where w_j and δ_j are the vertical and total deformations at hex mesh node j on the topmost layer, while $\hat{w}$ and $\hat{\delta}$ are the corresponding threshold values. Note that these constraints must be imposed at the end of each build-layer simulation. Unfortunately, this would result in an unacceptably large number of constraints; thus, constraint agglomeration is essential.

Commonly used agglomeration methods include p-norm [70,71], local relaxation functions [72,73], and Kreisselmeier–Steinhauser (KS) function [74,75]. Here, we use KS for constraint agglomeration as it provides a conservative estimate for the constraints. KS functions have widely been used in multi-load optimization [76] and with multiple objectives and constraints [77]. The KS agglomeration for the vertical and total deformations is given by

$$\begin{aligned} \kappa_1 &= \frac{1}{\rho_1} \ln\Big(\sum_{j=1}^{n} e^{\rho_1 w_j}\Big) \\ \kappa_2 &= \frac{1}{\rho_2} \ln\Big(\sum_{j=1}^{n} e^{\rho_2 \delta_j}\Big) \end{aligned} \tag{8}$$

where, ρ_1 and ρ_2 are the aggregation parameters. In the numerical experiments, the aggregation parameters ρ_1 and ρ_2 are set to $1/w_{max}$ and $1/\delta_{max}$ respectively, to ensure proper scaling. The hexmesh nodal deformation values in Eq. (7) can now be replaced by,

$$\begin{aligned} \kappa_1 &\leq \hat{w} \\ \kappa_2 &\leq \hat{\delta} \end{aligned} \tag{9}$$

2.3. Support optimization

2.3.1. Formulation

As the part and support evolve with the addition of new layers, the loads at the supports change. We therefore formulate the support optimization as a multi-load problem [78,79], where the part and supports are coupled and solved at each layer to compute deformations. The optimization problem is formulated as,

$$\min_{\{b_e\}} \quad V = \sum_{e=1}^{N} l_e t b_e$$

Subject to,

$$\begin{aligned} &\text{for } l = 1, 2, \ldots, m \\ &\frac{\kappa_1^l}{\hat{w}} - 1 \leq 0 \\ &\frac{\kappa_2^l}{\hat{\delta}} - 1 \leq 0 \\ &b^{min} \leq b_e \leq b^{max} \end{aligned} \tag{10}$$

where, V is the support volume (that is being minimized), N is the total number of frame members, t is the melt pool thickness, l_e and b_e are the

Table 1
Frame support parameters [7].

Frame parameters	Value	Units
Inter-comb distance (D)	0.6	mm
Part clearance height ($\hat{H}_{min}$)	5	mm
Comb height (C_h)	0.9	mm
Threshold support angle (θ_S)	50	degrees
Support angle for frame (θ_t)	35	degrees

Table 2
LPBF process and material parameters [7,80–82].

Process & material parameters	Value	Units
Material	SS316L	–
Melt pool thickness (t)	200	μm
Powder layer height (H)	45	μm
Young's modulus (Y)	62	GPa
Poisson's ratio (ν)	0.3	–
Shear modulus (G)	23.8	GPa
Inherent strain (ϵ^{inh})	[−0.00127 −0.00011 −0.0034]	–

lengths and extrusion widths of frame members respectively. The number of hex mesh layers m comprises layers corresponding to overhang surfaces as well as those from the heat-affected zone. The minimum bounds for frame member cross-section web length values(b^{min}) are defined based on smallest manufacturable feature size for a given set of printing parameters, while the maximum values (b^{max}), are set based on the total support volume. This ensures that no support member vanishes during the optimization and that the maximum assigned frame support volume does not exceed the total support volume. κ_1^l and κ_2^l are the KS function constraints for vertical deformation and total deformations of hex mesh nodes at the topmost layers l for each of the active coupled systems.

The sensitivities of objectives and constraints with respect to the design variables are derived in Appendix. For optimization, we use MATLAB's *fmincon* function with *sqp* algorithm.

2.4. Verification: Numerical experiments

The simulation parameters used in all experiments are first summarized.

2.4.1. Modeling parameters

The frame generation parameters chosen based on numerical and physical experiments [7] are summarized in Table 1. The inherent strain values for computing equivalent structural loads are based on SS316L [69,80–82], and are listed in Table 2.

The specimens are meshed with voxel elements, with element size equal to 10 times the powder layer height. The element size is based on minimum feature size, printer resolution, desired accuracy of results, and computational expenses [83–85].

2.4.2. Optimization parameters

As supports only affect the part deformations within a heat-affected zone (HAZ) [86], it is sufficient to consider the build process until the overhang surfaces, where supports are present; this significantly reduces the computational time. Support optimization is carried out for three different scenarios.

- *Vertical deformation constraint:* For the first set of experiments, only vertical deformation constraints $\hat{w}$ is imposed on each of the topmost layers, while total deformation constraint is not imposed. This constraint prevents re-coater collision.
- *Total deformation constraint*: Next, only a maximum total deformation $\hat{\delta}$ constraint is imposed on each topmost layer, while vertical deformation is not imposed. This helps achieve the desired geometric accuracy.
- *Vertical and total deformation constraint*: Finally, both the maximum vertical deformation $\hat{w}$ and maximum total deformation $\hat{\delta}$ constraints are imposed.

For all three scenarios, manufacturing constraints based on minimum achievable melt pool thickness and maximum support volume material are also imposed.

A commonly used double cantilever specimen [43,87,88] is first used to demonstrate the application of proposed approach. The part is placed on build plate and frame supports are generated for the overhang surfaces as shown in Fig. 9. As the part exhibits quarter symmetry, only a quarter model was used for simulation to speed up computation. Appropriate symmetric boundary conditions were imposed on the hexmesh nodes at the planes of symmetry. Three sets of experiments were conducted on the quarter model, first with only vertical deformation constraints, second with only total nodal deformation constraints and the third one with both vertical and total nodal deformation constraints. The optimized support significantly reduce maximum deformation of part as seen in Table 3. Standard block-type supports from Materialize Magics (Materialize NV, Leuven, Belgium) use close to 38% support volume for printing the double cantilever beam and also entrap metal powder within the support volume using SS316 material and manufacturer recommended parameters. The optimized frame supports the use of a similar amount of material for printing; however, the frame supports do not entrap any powder by virtue of their design.

2.5. Experiments on hemisphere

The next set of experiments is on the hemisphere (see Fig. 6); it has a convex overhang surface that requires evolving support. The part is placed 5 mm above the build plate and frame supports are generated with parameters listed in Table 1. It is meshed with hex elements and layer-wise loading using inherent strain-based load is applied on each of the active coupled system for structural deformation analysis. We consider two cases: relaxed constraints and tight constraints, and for each case, there are three scenarios, as discussed above.

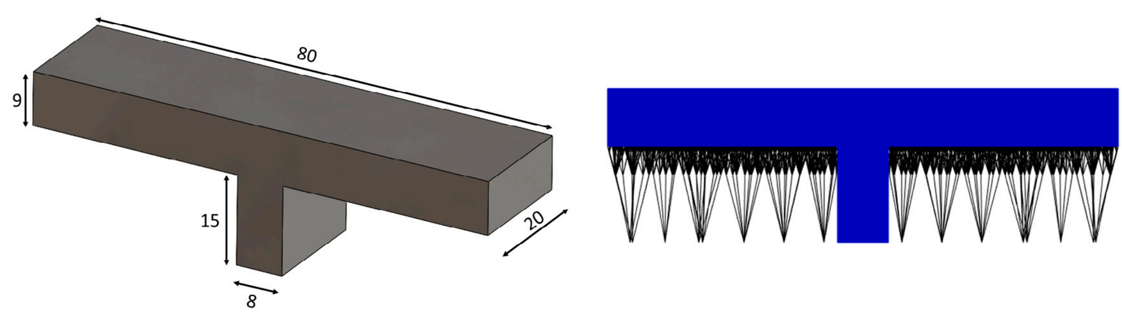

(a) *Part details (in mm)*   (b) *Part with Supports*

Fig. 9. Double-cantilever model.

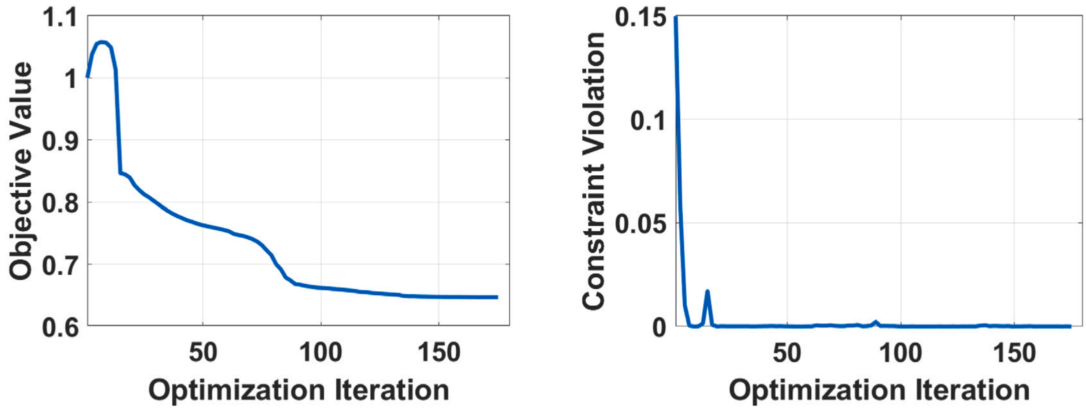

(a) *Objective Convergence* (b) *Constraint Convergence*

Fig. 10. Convergence history for hemisphere with vertical and total deformation constraints.

Table 3
Results for the double cantilever with deformation constraints.

Constraints	Initial V	Final V	Initial w_{max}	Final w_{max}	Initial δ_{max}	Final δ_{max}
$\hat{w}$ = 45 μm	75%	6.089%	27.67 μm	28.14 μm	334.53 μm	394.02 μm
$\hat{\delta}$ = 100 μm	75%	46.158%	27.67 μm	24.85 μm	334.53 μm	96.04 μm
$\hat{w}$ = 45 μm, $\hat{\delta}$ = 100 μm	75%	46.154%	27.67 μm	24.85 μm	334.53 μm	93.03 μm

Table 4
Results for the hemisphere with relaxed constraints.

Constraints	Initial V	Final V	Initial w_{max}	Final w_{max}	Initial δ_{max}	Final δ_{max}
$\hat{w}$ = 45 μm	30%	19.41%	51.53 μm	44.74 μm	59.06 μm	53.93 μm
$\hat{\delta}$ = 100 μm	30%	17.44%	51.53 μm	59.43 μm	59.06 μm	66.98 μm
$\hat{w}$ = 45 μm, $\hat{\delta}$ = 100 μm	30%	19.42%	51.53 μm	44.75 μm	59.06 μm	53.82 μm

Table 5
Results for the hemisphere with tighter constraints.

Constraints	Initial V	Final V	Initial w_{max}	Final w_{max}	Initial δ_{max}	Final δ_{max}
$\hat{w}$ = 45 μm	30%	19.408%	51.53 μm	44.74 μm	51.74 μm	45.0 μm
$\hat{\delta}$ = 50 μm	30%	20.873%	51.53 μm	42.07 μm	59.06 μm	49.71 μm
$\hat{w}$ = 45 μm, $\hat{\delta}$ = 50 μm	30%	20.873%	51.53 μm	42.07 μm	59.06 μm	49.71 μm

2.5.1. Relaxed constraints

The vertical deformation constraint $\hat{w}$ is set to 45 μm (powder layer height), while the total deformation constraint $\hat{\delta}$ is set to 100 μm. These are the maximum allowable deformation values for each of the hex mesh nodes on the top surface during layerwise build simulation. The value of 100 μm is based on the typical achievable part accuracy for the recommended set of material and process parameters [81]. The optimizer, initialized with 30% support volume, converges to a support volume fraction of close to 20% for all three scenarios. The convergence history for the third scenario is shown in Fig. 10; the optimization converges within 200 iterations. The convergence histories for the other three scenarios are quite similar. The optimizer takes close to 10 h for convergence. All optimization routines were run on a Windows 11 desktop with Intel(R) Core(TM) i7-12700KF CPU running at 3.31 GHz with 16 GB memory. Table 4 summarizes the results for the three different scenarios. The results indicate that for around 20% support volume, hemisphere can be printed with maximum nodal vertical deformation of 45 μm and maximum total deformation of 100 μm, for the given set of frame support, material and process parameters.

2.5.2. Tight constraints

For the same hemisphere specimen, we now set vertical deformation constraint $\hat{w}$ to 45 μm, and a tighter constraint on the total deformation $\hat{\delta}$ to 50 μm for higher geometric accuracy. The results for all three scenarios are summarized in Table 5. For relaxed constraint values, we observe that the vertical deformation constraint is dominating, while for the tighter constraint values, total deformation constraint guides the optimization results. Results for maximum layerwise deformation values for hemisphere with un-optimized and optimized frame supports are shown as an example in Fig. 11. The horizontal dotted line represents the maximum allowable deformation values, when tighter constraints were imposed.

2.6. Experiments on traffic cone

Next, we consider a traffic cone illustrated in Fig. 12(a); this part has a flat and a concave overhang surface, and also requires evolving supports. Frame supports are generated for the overhang surface and layerwise coupled structural analysis is performed to obtain nodal deformation values on the hex meshed part. Similar cases of constraints are tested on the traffic cone specimen.

2.6.1. Relaxed constraints

As before, maximum allowable vertical deformation($\hat{w}$) is set to 45 μm and maximum allowable total deformation($\hat{\delta}$) is set to 100 μm. Results for different scenarios of constraint imposition on the traffic cone are summarized in Table 6. The results highlight the role of manufacturing constraints. For all three scenarios, the optimal volume converges to the minimum material required for printing for the given frame supports, material and process parameters (see Table 6).

2.6.2. Tight constraints

Next, both the constraints are tighten with $\hat{w}$ set to 20 μm, and $\hat{\delta}$ to 25 μm. These tight constraints prevent recoater collision and generate higher part geometric accuracy. The results are presented in Table 7. Similar to the results for the hemisphere, the optimal support volume is sensitive to the constraints imposed. This can provide critical insights for the designer.

For the last experiment, the optimized supports with a 4-finned cross-section design for traffic cone specimen is shown in Fig. 13. Standard block type support from Materialize Magics (Materialize NV, Leuven, Belgium) uses 16.5% and 19.8% support volume for these two

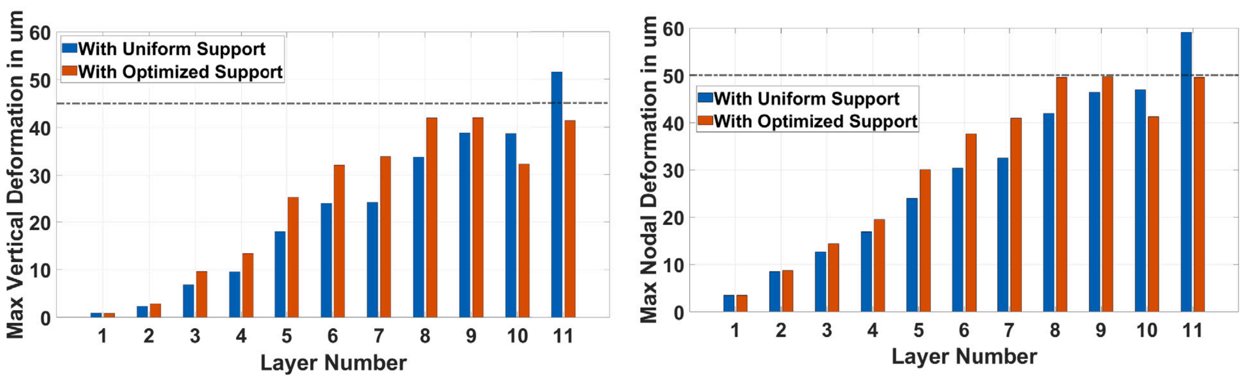

(a) *Layerwise Max Vertical Deformation* (b) *Layerwise Max Nodal Deformation*

Fig. 11. Layerwise maximum deformation variation with tighter constraints for hemisphere.

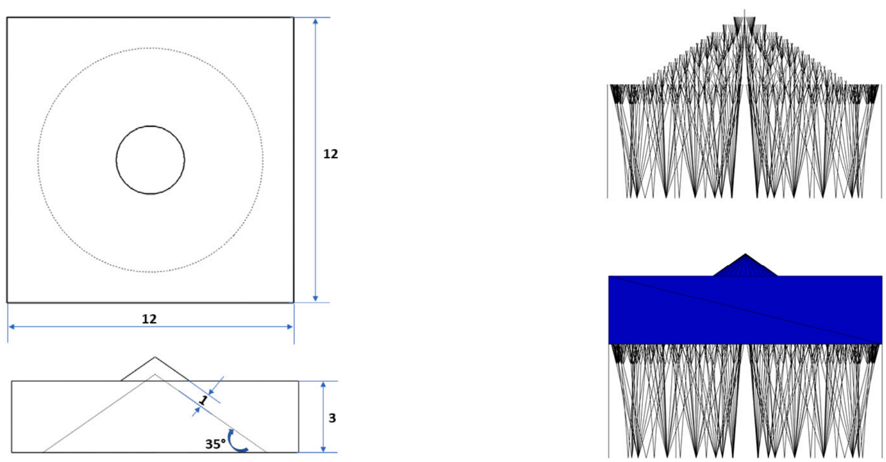

(a) *Part details* (b) *Frame support.*

Fig. 12. The traffic-cone model; dimensions are in mm.

Table 6
Results for the traffic cone with relaxed constraints.

Constraints	Initial V	Final V	Initial w_{max}	Final w_{max}	Initial δ_{max}	Final δ_{max}
$\hat{w}$ = 45 μm	30%	17.36%	17.49 μm	20.69 μm	25.23 μm	27.19 μm
$\hat{\delta}$ = 100 μm	30%	17.36%	17.49 μm	20.69 μm	25.23 μm	27.19 μm
$\hat{w}$ = 45 μm, $\hat{\delta}$ = 100 μm	30%	17.36%	17.49 μm	20.69 μm	25.23 μm	27.19 μm

Table 7
Results for the traffic cone with tighter constraints.

Constraints	Initial V	Final V	Initial w_{max}	Final w_{max}	Initial δ_{max}	Final δ_{max}
$\hat{w}$ = 20 μm	30%	17.55%	17.49 μm	19.70 μm	25.23 μm	27.00 μm
$\hat{\delta}$ = 25 μm	30%	20.54%	17.49 μm	16.72 μm	25.23 μm	24.34 μm
$\hat{w}$ = 20 μm, $\hat{\delta}$ = 25 μm	30%	20.54%	17.49 μm	16.72 μm	25.23 μm	24.34 μm

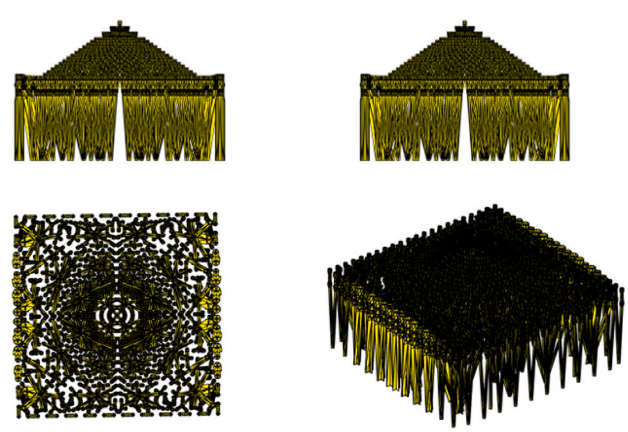

Fig. 13. Different views of optimized support with 4-finned design for traffic cone specimen.

parts respectively. However, the entrapped metal powders cannot be recovered [7]. The proposed framework optimizes support volume to around 20%, without any powder entrapment.

Commercial packages such as Materialize Magics (Materialize NV, Leuven, Belgium) have options for lattice/tree type supports, that do not entrap powders. However, additional support cones and blocks are manually added to areas with greater need. The support generation and optimization strategy discussed in this work automatically adds frame supports for overhang surfaces, and optimizes the cross-section area of these support members to constrain the part deformation at every layer.

3. Discussion and future work

A new strategy for optimizing frame supports to minimize part deformation through multi-load layerwise coupled part build analysis is proposed in this paper. The results from numerical experiments validate the framework for constraining part deformation through support structure optimization. The experiments also provided an optimal amount of support required to satisfy all the design and manufacturing constraints imposed.

The salient features of this strategy are:

- Layer-wise build process was captured through a multi-load formulation.
- Support and part were coupled and analyzed in tandem to represent the actual part-build process.
- An aggregation approach was used to impose vertical and total deformation constraints, while additional manufacturing constraint were also imposed.
- The support volume was optimized subject to these constraints.

The proposed framework is based on numerous simplifications and assumptions made for faster computations. However, there are potential sources of errors. Equivalent layer loading involves lumping multiple physical powder layers for ease of analysis. Furthermore, layer-wise loading on the topmost layer has been assumed, neglecting the role of laser scan patterns, geometric features, and different modes of heat transfer. The material properties have been assumed to be constant, i,e., independent of temperature. The framework considers linear elastic material that does not account for anisotropy.

Some of these shortcomings can potentially be addressed in future work. The framework can be extended to include elasto-plasticity models through parallel computing [25]. The frame topology has been assumed to be fixed, however, an optimal topology can further reduce the amount of support needed. The framework needs to be validated for parts requiring internal and external supports. The validations of numerically predicted layer-wise part deformation through physical experiments is important but non-trivial.

CRediT authorship contribution statement

Subodh C. Subedi: Writing – review & editing, Writing – original draft, Software, Methodology, Formal analysis, Data curation, Conceptualization. **Dan J. Thoma:** Writing – review & editing. **Krishnan Suresh:** Writing – review & editing, Writing – original draft, Methodology, Funding acquisition, Formal analysis, Conceptualization.

Declaration of competing interest

The authors declare that they do not have any conflict of interest by submitting this paper. Further, this paper has not been submitted to any other journal or conference.

Data availability

No data was used for the research described in the article.

Acknowledgments

This work was funded through Technical Data Analysis Inc. (TDA) SBIR contract N00030-18-C-0239 and STTR contract N68335-19-570-C-0321. DJT would like to acknowledge support of the US National Science Foundation (NSF) grant 1941206.

Appendix. Sensitivity computation

Here, we summarize the sensitivity equations required for gradient-driven optimization.

A.1. Scaling

For numerical stability and robustness, various quantities are scaled with a scaling variable x_e as follows.

$$x_e = \frac{b_e}{b_{e\_initial}} \tag{11}$$

where, $b_{e\_initial}$ are the web lengths (see Fig. 7), and b_e are the updated extrusion lengths at every optimization iteration. The objective is scaled

$$\phi = \frac{\sum_{e=1}^{N} l_e t b_e}{V} \tag{12}$$

where V is the initial support volume. Similarly, the constraints are scaled as follows:

$$\begin{aligned} g_1 &: \frac{\kappa_1^l}{\hat{w}} - 1 \le 0 \\ g_2 &: \frac{\kappa_2^l}{\hat{\delta}} - 1 \le 0 \end{aligned} \tag{13}$$

A.2. Sensitivity

The sensitivity of objective function is given by,

$$\frac{\partial \phi}{\partial x_e} = \frac{l_e t}{V} b_{e\_initial} \tag{14}$$

A.2.1. Vertical deformation constraint sensitivity

$$\frac{\partial g_1}{\partial x_e} = \frac{1}{\hat{w}} \frac{\partial \kappa_1}{\partial x_e} \tag{15}$$

Expanding the RHS of Eq. (15),

$$\begin{aligned} \frac{\partial \kappa_1}{\partial x_e} &= (\frac{\partial \kappa_1}{\partial u_1}\frac{\partial w_1}{\partial b_e} + \frac{\partial \kappa_1}{\partial w_2}\frac{\partial w_2}{\partial b_e} + \cdots ..) b_{e\_initial} \\ &= (\nabla_w \kappa_1)^T [\frac{\partial w_j}{\partial b_e}] b_{e\_initial} \end{aligned} \tag{16}$$

$$\begin{aligned} \nabla_w \kappa_1 = \frac{\partial \kappa_1}{\partial w_j} &= \frac{1}{\rho_1 (\sum_{j=1}^{n} e^{\rho_1 w_j})} \frac{\rho e^{\rho_1 w_j}}{w_j} \\ \frac{\partial \kappa_1}{\partial w_j} &= \frac{e^{\rho w_j}}{w_j (\sum_{j=1}^{n} e^{\rho_1 w_j})} \end{aligned} \tag{17}$$

Using the state equation and taking its derivative against the extrusion width,

$$\begin{aligned} K\delta &= F \\ \frac{\partial w}{\partial b_e} &= -K^{-1} \frac{\partial K}{\partial b_e} w \end{aligned} \tag{18}$$

Substituting $\frac{\partial w}{\partial b_e}$ from Eq. (18) into Eq. (16),

$$\begin{aligned} \frac{\partial g_1}{\partial x_e} &= \frac{1}{\hat{w}} \frac{\partial \kappa_1}{\partial x_e} \\ &= \frac{1}{\hat{w}} (\nabla_w \kappa_1)^T [\frac{\partial w_j}{\partial b_e}] b_{e\_initial} \\ &= \frac{1}{\hat{w}} (\nabla_w \kappa_1)^T [-K^{-1} \frac{\partial K}{\partial b_e} w_j] b_{e\_initial} \end{aligned} \tag{19}$$

Consider an adjoint problem to efficiently compute the constraint sensitivity,

$$K\lambda_1 = \nabla_w \kappa_1 \tag{20}$$

where, λ_1 are the adjoint variables.

Combining Eqs. (19) and (20),

$$\frac{\partial g_1}{\partial x_e} = \frac{-\lambda_1^T}{\hat{w}} [\frac{\partial K}{\partial b_e} w_j] b_{e\_initial} \tag{21}$$

A.2.2. Total deformation constraint sensitivity

$$\frac{\partial g_2}{\partial x_e} = \frac{1}{\hat{\delta}}\frac{\partial \kappa_2}{\partial x_e} \tag{22}$$

$$\begin{aligned}\frac{\partial \kappa_2}{\partial x_e} &= (\frac{\partial \kappa_2}{\partial u_1}\frac{\partial u_1}{\partial b_e} + \frac{\partial \kappa_2}{\partial v_1}\frac{\partial v_1}{\partial b_e} + \frac{\partial \kappa_2}{\partial w_1}\frac{\partial w_1}{\partial b_e} + \cdots)b_{e\_initial} \\ &= (\nabla_\delta \kappa_2)^T[\frac{\partial \delta_j}{\partial b_e}]b_{e\_initial}\end{aligned} \tag{23}$$

$$\nabla_\delta \kappa_2 = [\frac{\partial \kappa_2}{\partial u_1}\,\frac{\partial \kappa_2}{\partial v_1}\,\frac{\partial \kappa_2}{\partial w_1}\,\frac{\partial \kappa}{\partial u_2}\cdots] \tag{24}$$

From the definition of KS functions,

$$\begin{aligned}\frac{\partial \kappa_2}{\partial u_j} &= \frac{u_j e^{\rho_2 \delta_j}}{\delta_j(\sum_{j=1}^{n} e^{\rho_2 \delta_j})} \\ \frac{\partial \kappa_2}{\partial v_j} &= \frac{v_j e^{\rho_2 \delta_j}}{\delta_j(\sum_{j=1}^{n} e^{\rho_2 \delta_j})} \\ \frac{\partial \kappa_2}{\partial w_j} &= \frac{w_j e^{\rho_2 \delta_j 5}}{\delta_j(\sum_{j=1}^{n} e^{\rho_2 \delta_j})}\end{aligned} \tag{25}$$

Using the state equation and taking its derivative against the extrusion width,

$$\begin{aligned}K\delta &= F \\ \frac{\partial \delta}{\partial b_e} &= -K^{-1}\frac{\partial K}{\partial b_e}\delta\end{aligned} \tag{26}$$

Substituting Eq. (26) into Eq. (23), we get,

$$\begin{aligned}\frac{\partial g_2}{\partial x_e} &= \frac{1}{\hat{\delta}}\frac{\partial \kappa_2}{\partial x_e} \\ &= \frac{1}{\hat{\delta}}(\nabla_\delta \kappa_2)^T[\frac{\partial \delta_j}{\partial b_e}]b_{e\_initial} \\ &= \frac{1}{\hat{\delta}}(\nabla_\delta \kappa_2)^T[-K^{-1}\frac{\partial K}{\partial b_e}\delta_j]b_{e\_initial}\end{aligned} \tag{27}$$

Consider an adjoint problem to efficiently compute the constraint sensitivity,

$$\nabla_\delta \kappa_2 = K\lambda_2 \tag{28}$$

where, λ_2 are the adjoint variables.

Combining Eqs. (27) and (28),

$$\frac{\partial g_2}{\partial x_e} = -\frac{\lambda_2^T}{\hat{\delta}}[\frac{\partial K}{\partial b_e}\delta_j]b_{e_{initial}} \tag{29}$$

References

[1] NC Levkulich, SL Semiatin, JE Gockel, JR Middendorf, AT DeWald, NW Klingbeil, The effect of process parameters on residual stress evolution and distortion in the laser powder bed fusion of Ti-6Al-4V, Addit. Manuf. 28 (2019) 475–484.
[2] Y.P. Yang, M. Jamshidinia, P. Boulware, S.M. Kelly, Prediction of microstructure, residual stress, and deformation in laser powder bed fusion process, Comput. Mech. 61 (2018) 599–615.
[3] Shanshan Zhang, B. Lane, J. Whiting, Kevin Chou, An investigation into metallic powder thermal conductivity in laser powder bed fusion additive manufacturing, in: Proceedings of the Solid Freeform Fabrication (SFF) Symposium, Austin, TX, Vol. 29, 2018, pp. 1796–1807.
[4] Mattia Mele, Giampaolo Campana, André Bergmann, Optimisation of part orientation and design of support structures in laser powder bed fusion, Int. J. Interact. Des. Manuf. (IJIDeM) 16 (2) (2022) 597–611.
[5] Behzad Rankouhi, Dan J. Thoma, Krishnan Suresh, Support structure design for selective laser melting process, in: Manufacturing in the Era of 4th Industrial Revolution: A World Scientific Reference Volume 1: Recent Advances in Additive Manufacturing, World Scientific, 2020, pp. 9–40.
[6] Kai Zeng, Deepankar Pal, Chong Teng, Brent E. Stucker, Evaluations of effective thermal conductivity of support structures in selective laser melting, Addit. Manuf. 6 (2015) 67–73.
[7] Subodh C Subedi, Ahmad Shahba, Mythili Thevamaran, Dan J Thoma, Krishnan Suresh, Towards the optimal design of support structures for laser powder bed fusion-based metal additive manufacturing via thermal equivalent static loads, Addit. Manuf. 57 (2022) 102956.
[8] Subodh C. Subedi, Dan J. Thoma, Krishnan Suresh, Optimal truss-type supports for minimal part distortion in LPBF, in: Proceedings of the Solid Freeform Fabrication Symposium (SFF), Austin, TX, University of Texas at Austin, 2022.
[9] Alexandru Paraschiv, Gheorghe Matache, Nicolae Constantin, Mihai Vladut, Investigation of scanning strategies and laser remelting effects on top surface deformation of additively manufactured IN 625, Materials 15 (9) (2022) 3198.
[10] Prabhat Pant, Filomena Salvemini, Sebastian Proper, Vladimir Luzin, Kjell Simonsson, Sören Sjöström, Seyed Hosseini, Ru Lin Peng, Johan Moverare, A study of the influence of novel scan strategies on residual stress and microstructure of L-shaped LPBF IN718 samples, Mater. Des. 214 (2022) 110386.
[11] Panagis Foteinopoulos, Alexios Papacharalampopoulos, Konstantinos Angelopoulos, Panagiotis Stavropoulos, Development of a simulation approach for laser powder bed fusion based on scanning strategy selection, Int. J. Adv. Manuf. Technol. 108 (2020) 3085–3100.
[12] Lin Cheng, Albert To, Part-scale build orientation optimization for minimizing residual stress and support volume for metal additive manufacturing: Theory and experimental validation, Comput. Aided Des. 113 (2019) 1–23.
[13] Zhibo Luo, Fan Yang, Guoying Dong, Yunlong Tang, Yaoyao Fiona Zhao, Orientation optimization in layer-based additive manufacturing process, in: International Design Engineering Technical Conferences and Computers and Information in Engineering Conference, Vol. 50077, American Society of Mechanical Engineers, 2016, V01AT02A039.
[14] Sumanth Theeda, Shweta Hanmant Jagdale, Bharath Bhushan Ravichander, Golden Kumar, Optimization of process parameters in laser powder bed fusion of SS 316L parts using artificial neural networks, Metals 13 (5) (2023) 842.
[15] Christian Knaak, Lukas Masseling, Emil Duong, Peter Abels, Arnold Gillner, Improving build quality in laser powder bed fusion using high dynamic range imaging and model-based reinforcement learning, IEEE Access 9 (2021) 55214–55231.
[16] AM software extends capabilities, Met. Powder Rep. 74 (4) (2019) 208.
[17] Sebastian Weber, Joaquin Montero, Matthias Bleckmann, Kristin Paetzold, Support-free metal additive manufacturing: a structured review on the state of the art in academia and industry, Proc. Des. Soc. 1 (2021) 2811–2820.
[18] Jennifer Coyne, Barnes John, I want to break free: The journey towards reducing or eliminating support structures in Additive Manufacturing, Met. AM 7 (3) (2021) 155–163.
[19] Guido A.O. Adam, Detmar Zimmer, Design for Additive Manufacturing—Element transitions and aggregated structures, CIRP J. Manuf. Sci. Technol. 7 (1) (2014) 20–28.
[20] Botao Zhang, Lun Li, Sam Anand, Distortion prediction and NURBS based geometry compensation for reducing part errors in additive manufacturing, Procedia Manuf. 48 (2020) 706–717.
[21] Tao Liu, Cody S Lough, Hossein Sehhat, Yi Ming Ren, Panagiotis D Christofides, Edward C Kinzel, Ming C Leu, In-situ infrared thermographic inspection for local powder layer thickness measurement in laser powder bed fusion, Addit. Manuf. 55 (2022) 102873.
[22] Mihaela L Vlasea, Brandon Lane, Felipe Lopez, Sergey Mekhontsev, A Donmez, Development of powder bed fusion additive manufacturing test bed for enhanced real-time process control, in: Proceedings of the Solid Freeform Fabrication Symposium (SFF), Austin, TX, University of Texas at Austin, 2015.
[23] Jennifer Bracken, Thomas Pomorski, Clinton Armstrong, Rohan Prabhu, Timothy W Simpson, Kathryn Jablokow, William Cleary, Nicholas A Meisel, Design for metal powder bed fusion: The geometry for additive part selection (GAPS) worksheet, Addit. Manuf. 35 (2020) 101163.
[24] Xuan Liang, Wen Dong, Qian Chen, Albert C. To, On incorporating scanning strategy effects into the modified inherent strain modeling framework for laser powder bed fusion, Addit. Manuf. 37 (2021) 101648.
[25] Dirk Munro, Can Ayas, Matthijs Langelaar, Fred van Keulen, On process-step parallel computability and linear superposition of mechanical responses in additive manufacturing process simulation, Addit. Manuf. 28 (2019) 738–749.
[26] Xuan Liang, Devlin Hayduke, Albert C. To, An enhanced layer lumping method for accelerating simulation of metal components produced by laser powder bed fusion, Addit. Manuf. 39 (2021) 101881.
[27] Matthijs Langelaar, Topology optimization for additive manufacturing with controllable support structure costs, in: 7th European Congress on Computational Methods in Applied Sciences and Engineering, National Technical University of Athens (NTUA), Greece, 2016, pp. 3689–3699.
[28] Woo-Seok Choi, Gyung-Jin Park, Structural optimization using equivalent static loads at all time intervals, Comput. Methods Appl. Mech. Engrg. 191 (19–20) (2002) 2105–2122.
[29] Woo-Seok Choi, Keun-Bae Park, Gyung-Jin Park, Calculation of equivalent static loads and its application, Nucl. Eng. Des. 235 (22) (2005) 2337–2348.
[30] Amir M. Mirzendehdel, Krishnan Suresh, Support structure constrained topology optimization for additive manufacturing, Comput. Aided Des. 81 (2016) 1–13.
[31] Yu-Hsin Kuo, Chih-Chun Cheng, Yang-Shan Lin, Cheng-Hung San, Support structure design in additive manufacturing based on topology optimization, Struct. Multidiscip. Optim. 57 (1) (2018) 183–195.
[32] Francesco Mezzadri, Vladimir Bouriakov, Xiaoping Qian, Topology optimization of self-supporting support structures for additive manufacturing, Addit. Manuf. 21 (2018) 666–682.

[33] Grégoire Allaire, Martin Bihr, Beniamin Bogosel, Support optimization in additive manufacturing for geometric and thermo-mechanical constraints, Struct. Multidiscip. Optim. 61 (6) (2020) 2377–2399.
[34] Kailun Hu, Shuo Jin, Charlie C.L. Wang, Support slimming for single material based additive manufacturing, Comput. Aided Des. 65 (2015) 1–10.
[35] H.R. Javidrad, F. Javidrad, Review of state-of-the-art research on the design and manufacturing of support structures for powder-bed fusion additive manufacturing, Prog. Addit. Manuf. (2023) 1–26.
[36] Mingdong Zhou, Yichang Liu, Zhongqin Lin, Topology optimization of thermal conductive support structures for laser additive manufacturing, Comput. Methods Appl. Mech. Engrg. 353 (2019) 24–43.
[37] Sebastian Weber, Joaquin Montero, Matthias Bleckmann, Kristin Paetzold, Parametric design optimisation of tree-like support structure for the laser-based powder bed fusion of metals, J. Manuf. Process. 84 (2022) 660–668.
[38] Grégoire Allaire, Beniamin Bogosel, Optimizing supports for additive manufacturing, Struct. Multidiscip. Optim. 58 (6) (2018) 2493–2515.
[39] Cunfu Wang, Xiaoping Qian, Optimizing support for heat dissipation in additive manufacturing, in: International Design Engineering Technical Conferences and Computers and Information in Engineering Conference, Vol. 83983, American Society of Mechanical Engineers, 2020, V009T09A018.
[40] Ehsan Malekipour, Andres Tovar, Hazim El-Mounayri, Heat conduction and geometry topology optimization of support structure in laser-based additive manufacturing, in: Mechanics of Additive and Advanced Manufacturing, Volume 9: Proceedings of the 2017 Annual Conference on Experimental and Applied Mechanics, Springer, 2018, pp. 17–27.
[41] Jeroen Pellens, Geert Lombaert, Manuel Michiels, Tom Craeghs, Mattias Schevenels, Topology optimization of support structure layout in metal-based additive manufacturing accounting for thermal deformations, Struct. Multidiscip. Optim. 61 (2020) 2291–2303.
[42] Renkai Huang, Ning Dai, Xiaosheng Cheng, Lei Wang, Topology optimization of lattice support structures for heat conduction in selective laser melting, Int. J. Adv. Manuf. Technol. 109 (2020) 1841–1851.
[43] Lin Cheng, Xuan Liang, Jiaxi Bai, Qian Chen, John Lemon, Albert To, On utilizing topology optimization to design support structure to prevent residual stress induced build failure in laser powder bed metal additive manufacturing, Addit. Manuf. 27 (2019) 290–304.
[44] Eilam Amir, Oded Amir, Concurrent high-resolution topology optimization of structures and their supports for additive manufacturing, Struct. Multidiscip. Optim. 63 (6) (2021) 2589–2612.
[45] Katharina Bartsch, Fritz Lange, Melanie Gralow, Claus Emmelmann, Novel approach to optimized support structures in laser beam melting by combining process simulation with topology optimization, J. Laser Appl. 31 (2) (2019) 022302.
[46] Takao Miki, Shinji Nishiwaki, Topology optimization of the support structure for heat dissipation in additive manufacturing, Finite Elem. Anal. Des. 203 (2022) 103708.
[47] Zhi-Dong Zhang, Osezua Ibhadode, Usman Ali, Chinedu Francis Dibia, Pouyan Rahnama, Ali Bonakdar, Ehsan Toyserkani, Topology optimization parallel-computing framework based on the inherent strain method for support structure design in laser powder-bed fusion additive manufacturing, Int. J. Mech. Mater. Des. 16 (2020) 897–923.
[48] Kang-Hyun Lee, Gun Jin Yun, Design optimization of thermally conductive support structure for laser powder-bed fusion process with part-scale thermal history, Addit. Manuf. 51 (2022) 102627.
[49] Florian Dugast, Albert C. To, Topology optimization of support structures in metal additive manufacturing with elastoplastic inherent strain modeling, Struct. Multidiscip. Optim. 66 (5) (2023) 105.
[50] Subodh C. Subedi, Chaman Singh Verma, Krishnan Suresh, A review of methods for the geometric post-processing of topology optimized models, J. Comput. Inf. Sci. Eng. 20 (6) (2020).
[51] Yong Zhou, Han Lu, Qingrong Ren, Yang Li, Generation of a tree-like support structure for fused deposition modelling based on the L-system and an octree, Graph. Models 101 (2019) 8–16.
[52] Juraj Vanek, Jorge A. Garcia Galicia, Bedrich Benes, Clever support: Efficient support structure generation for digital fabrication, in: Computer Graphics Forum, vol. 33, Wiley Online Library, 2014, pp. 117–125.
[53] Andrés Díaz Lantada, Adrián de Blas Romero, Álvaro Sánchez Isasi, Diego Garrido Bellido, Design and performance assessment of innovative eco-efficient support structures for additive manufacturing by photopolymerization, J. Ind. Ecol. 21 (S1) (2017) S179–S190.
[54] Walter D. Pilkey, Analysis and Design of Elastic Beams: Computational Methods, John Wiley & Sons, 2002.
[55] Ibiye Aseibichin Roberts, CJ Wang, R Esterlein, M Stanford, DJ Mynors, A three-dimensional finite element analysis of the temperature field during laser melting of metal powders in additive layer manufacturing, Int. J. Mach. Tools Manuf. 49 (12–13) (2009) 916–923.
[56] Mohamad Bayat, Christopher G Klingaa, Sankhya Mohanty, David De Baere, Jesper Thorborg, Niels S Tiedje, Jesper H Hattel, Part-scale thermo-mechanical modelling of distortions in Laser Powder Bed Fusion–Analysis of the sequential flash heating method with experimental validation, Addit. Manuf. 36 (2020) 101508.
[57] Michael Gouge, Erik Denlinger, Jeff Irwin, Chao Li, Pan Michaleris, Experimental validation of thermo-mechanical part-scale modeling for laser powder bed fusion processes, Addit. Manuf. 29 (2019) 100771.
[58] Pedro Alvarez, Joseba Ecenarro, Iñaki Setien, Maria San Sebastian, Alberto Echeverria, Luka Eciolaza, Computationally efficient distortion prediction in powder bed fusion additive manufacturing, Int. J. Eng. Res. Sci. 2 (10) (2016) 39–46.
[59] Iñaki Setien, Michele Chiumenti, Sjoerd van der Veen, Maria San Sebastian, Fermín Garciandía, Alberto Echeverría, Empirical methodology to determine inherent strains in additive manufacturing, Comput. Math. Appl. 78 (7) (2019) 2282–2295.
[60] Nils Keller, Vasily Ploshikhin, New method for fast predictions on residual stress and distortion of AM parts, in: Proceedings of the Solid Freeform Fabrication Symposium (SFF), Austin, TX, University of Texas at Austin, 2014.
[61] H. Murakawa, Inherent strain as an interface between computational welding mechanics and its industrial application, Math. Model. Weld Phenom. 4 (1998) 597–619.
[62] M.G. Yuan, Y. Ueda, Prediction of residual stresses in welded T-and I-joints using inherent strains, 1996.
[63] Hossein Mohammadtaheri, Ramin Sedaghati, Marjan Molavi-Zarandi, Inherent strain approach to estimate residual stress and deformation in the laser powder bed fusion process for metal additive manufacturing—a state-of-the-art review, Int. J. Adv. Manuf. Technol. 122 (5–6) (2022) 2187–2202.
[64] Jiangchao Wang, Sherif Rashed, Hidekazu Murakawa, Mechanism investigation of welding induced buckling using inherent deformation method, Thin-Walled Struct. 80 (2014) 103–119.
[65] Wen Dong, Xuan Liang, Qian Chen, Shawn Hinnebusch, Zekai Zhou, Albert C To, A new procedure for implementing the modified inherent strain method with improved accuracy in predicting both residual stress and deformation for laser powder bed fusion, Addit. Manuf. 47 (2021) 102345.
[66] Xuan Liang, Lin Cheng, Qian Chen, Qingcheng Yang, Albert C To, A modified method for estimating inherent strains from detailed process simulation for fast residual distortion prediction of single-walled structures fabricated by directed energy deposition, Addit. Manuf. 23 (2018) 471–486.
[67] Qingcheng Yang, Pu Zhang, Lin Cheng, Zheng Min, Minking Chyu, Albert C To, Finite element modeling and validation of thermomechanical behavior of Ti-6Al-4V in directed energy deposition additive manufacturing, Addit. Manuf. 12 (2016) 169–177.
[68] M.P. Fransen, Eigenstrain reconstruction of residual stresses induced by selective laser melting, 2016.
[69] Hong-Seok Park, Hwa Seon Shin, Ngoc-Hien Tran, A new approach for calculating inherent strain and distortion in additive manufacturing of metal parts, Int. J. Adv. Manuf. Technol. 121 (9–10) (2022) 6507–6521.
[70] Pierre Duysinx, Ole Sigmund, New developments in handling stress constraints in optimal material distribution, in: 7th AIAA/USAF/NASA/ISSMO Symposium on Multidisciplinary Analysis and Otimization, 1998, p. 4906.
[71] G.Y. Qiu, X.S. Li, A note on the derivation of global stress constraints, Struct. Multidiscip. Optim. 40 (2010) 625–628.
[72] Grégoire Allaire, François Jouve, Hervé Maillot, Topology optimization for minimum stress design with the homogenization method, Struct. Multidiscip. Optim. 28 (2004) 87–98.
[73] Pierre Duysinx, Martin P. Bendsøe, Topology optimization of continuum structures with local stress constraints, Internat. J. Numer. Methods Engrg. 43 (8) (1998) 1453–1478.
[74] Gerhard Kreisselmeier, Reinhold Steinhauser, Application of vector performance optimization to a robust control loop design for a fighter aircraft, Internat. J. Control 37 (2) (1983) 251–284.
[75] Chau Le, Julian Norato, Tyler Bruns, Christopher Ha, Daniel Tortorelli, Stress-based topology optimization for continua, Struct. Multidiscip. Optim. 41 (2010) 605–620.
[76] Mehmet A Akgun, Raphael T Haftka, K Chauncey Wu, Joanne L Walsh, John H Garcelon, Efficient structural optimization for multiple load cases using adjoint sensitivities, AIAA J. 39 (3) (2001) 511–516.
[77] JR.R.A. Martins, Nicholas M.K. Poon, On structural optimization using constraint aggregation, in: VI World Congress on Structural and Multidisciplinary Optimization WCSMO6, Rio de Janeiro, Brasil, Citeseer, 2005.
[78] Yongxin Li, Quanwei Yang, Tao Chang, Tao Qin, Fenghe Wu, Multi-load cases topological optimization by weighted sum method based on load case severity degree and ideality, Adv. Mech. Eng. 12 (8) (2020) 1687814020947510.
[79] J. Lógó, B. Balogh, E. Pintér, Topology optimization considering multiple loading, Comput. Struct. 207 (2018) 233–244.
[80] Thoufeili Taufek, Yupiter HP Manurung, Stephan Lüder, Marcel Graf, Farrahshaida Mohd Salleh, Distortion analysis of SLM product of SS316l using inherent strain method, in: IOP Conference Series: Materials Science and Engineering, Vol. 834, IOP Publishing, 2020, 012011.
[81] EOS, EOS stainless steel 316L material data sheet, 2022.
[82] Kai Guo, Zhicheng Huang, Yongqiang Tu, Yifan Qie, Lihong Qiao, Nabil Anwer, Improved inherent strain extraction algorithm based analytical surface modeling for Ti-6Al-4V and SS316l selective laser melting part, J. Manuf. Process. 101 (2023) 618–638.

[83] Yicha Zhang, Alain Bernard, Generic build time estimation model for parts produced by SLS, in: High Value Manufacturing: Advanced Research in Virtual and Rapid Prototyping. Proceedings of the 6th International Conference on Advanced Research in Virtual and Rapid Prototyping, 2013, pp. 43–48.
[84] Saish Tedia, Christopher B. Williams, Manufacturability analysis tool for additive manufacturing using voxel-based geometric modeling, in: Proceedings of the Solid Freeform Fabrication (SFF) Symposium, Austin, TX, 2016, pp. 3–22.
[85] Thomas Mayer, Gabriel Brändle, Andreas Schönenberger, Robert Eberlein, Simulation and validation of residual deformations in additive manufacturing of metal parts, Heliyon 6 (5) (2020) e03987.
[86] Jingjing Yang, Jie Han, Hanchen Yu, Jie Yin, Ming Gao, Zemin Wang, Xiaoyan Zeng, Role of molten pool mode on formability, microstructure and mechanical properties of selective laser melted Ti-6Al-4V alloy, Mater. Des. 110 (2016) 558–570.
[87] Qian Chen, Xuan Liang, Devlin Hayduke, Jikai Liu, Lin Cheng, Jason Oskin, Ryan Whitmore, Albert C To, An inherent strain based multiscale modeling framework for simulating part-scale residual deformation for direct metal laser sintering, Addit. Manuf. 28 (2019) 406–418.
[88] A Kiran, J Hodek, J Vavřík, M Brázda, M Urbánek, J Cejpek, Design & modelling of double cantilever structure by stainless steel 316L deposited using additive manufacturing directed energy deposition process, in: IOP Conference Series: Materials Science and Engineering, Vol. 1178, IOP Publishing, 2021, 012027.